

Fermi Surface Nesting and the Origin of the Charge Density Wave in NbSe₂

M.D. Johannes, I.I. Mazin, C.A. Howells

Code 6391, Naval Research Laboratory, Washington, D.C. 20375

We use highly accurate density functional calculations to study the band structure and Fermi surfaces of NbSe₂. We calculate the real part of the non-interacting susceptibility, $\Re\chi_0(\mathbf{q})$, which is the relevant quantity for a charge density wave (CDW) instability and the imaginary part, $\Im\chi_0(\mathbf{q})$, which directly shows Fermi surface (FS) nesting. We show that there are very weak peaks in $\Re\chi_0(\mathbf{q})$ near the CDW wave vector, but that no such peaks are visible in $\Im\chi_0(\mathbf{q})$, definitively eliminating FS nesting as a factor in CDW formation. Because the peak in $\Re\chi_0(\mathbf{q})$ is broad and shallow, it is unlikely to be the direct cause of the CDW instability. We briefly address the possibility that electron-electron interactions (local field effects) produce additional structure in the total (renormalized) susceptibility, and we discuss the role of electron-ion matrix elements.

In 1964 V.L. Ginzburg proposed excitonic superconductivity in quasi-2D structures¹ composed of metal layers sandwiched between insulating layers. By that time, only two layered materials were known to be superconducting,^{2,3} PdTe₂ and NbSe₂. In the four decades since then, NbSe₂ and isostructural selenides have been intensively investigated (close to 1.5 thousand papers published to date). However, the main interest in this compound has shifted from the fact that it is a layered material (hundreds of layered superconductors are now known), to the existence of a nearly-commensurate charge density wave (CDW)⁴ instability and its possible interplay with the superconductivity that sets in at a lower temperature. We mainly forego discussion of the interesting issues surrounding the superconducting state, its origin, and its relationship to the CDW state, and instead concentrate on the mechanism behind the CDW transition itself.

The first electronic structure calculations for NbSe₂ were presented by Mattheiss in 1973⁵. Using a non-self-consistent potential he was able to produce a band structure with basic features in reasonable agreement with more recent self-consistent calculations^{6,7,8}, but which showed only two bands crossing the Fermi energy (it is now known that there are three), and underestimated the energy depth of a saddle point at $\sim \frac{1}{2} \Gamma K$. Fermi surfaces based on this band structure led to early suggestions that the CDW transition was driven by nesting⁴, an assumption that has carried through to the present time. The nearness of the saddle point to the Fermi energy (E_F) led Rice and Scott⁹ to argue that CDW formation was driven, not by Fermi surface (FS) nesting in the conventional sense, but rather by saddle points lying within $k_B T_{CDW}$ of E_F and separated by the CDW wavevector, $\mathbf{Q}_{CDW} = (\frac{1}{3}, 0, 0)$. A significant amount of effort has been spent on resolving the ‘controversy’ between the nesting and saddle point theories for NbSe₂ and for related CDW compounds such as 2H-TaSe₂, 1T-TaSe₂, TaS₂ and others, but no specific feature that would give rise to an instability at \mathbf{Q}_{CDW} has been convincingly isolated. As early as 1978, Doran *et al*^{10,11} used a simple one-band tight-binding model to show that the susceptibility has no sharp peaks of electronic origin and

made a rudimentary calculation of the electron-ion matrix elements that suggested strong coupling at \mathbf{Q}_{CDW} . Nonetheless, in the more modern era of self-consistent calculations, the FS nesting and saddle point hypotheses continue to be debated and FS nesting is cited as a contributing factor in CDW formation in almost every paper that addresses the issue. In this paper we report a quantitative analysis of the non-interacting susceptibility, $\chi_0(\mathbf{q}, \omega = 0)$, based on first principles density functional theory (DFT) calculations, and show that not only is the structure in momentum space extremely weak, but that FS nesting does not play any role at all and can be definitively ruled out as a cause for CDW formation. Instead, we argue, the instability must be due to the electron-ion interaction, or possibly from local field effects. The structure of the paper is as follows: In Section I, we lay out the basic mathematical framework for dielectric calculations, and discuss the various approximations we employ. In Section II, we present and discuss the calculated band structure and Fermi surfaces and show that there is good agreement with experiment. In Section III, we show the real and imaginary parts of the non-interacting susceptibility, and discuss the origins of prominent features, emphasizing the lack of a strong peak at the CDW wave vector and the irrelevance of FS nesting.

I. GENERAL THEORY

A material is unstable toward the formation of a CDW at wave vector \mathbf{Q} when the response function (inverse electronic dielectric function) fails to satisfy the stability condition¹²,

$$\epsilon^{-1}(\mathbf{Q}, 0) = 1 + V_C(Q)\chi(\mathbf{Q}, 0) \leq 1 \quad (1)$$

where $V_C(q) = 4\pi e^2/q^2$ is the Coulomb potential, and the susceptibility $\chi(\mathbf{q}, 0)$ is normally negative. A dielectric constant within the range $0 \leq \epsilon(\mathbf{Q}, \omega) < 1$ therefore signals a CDW instability and, in conjunction with Eq. 1, indicates that the latter range is accessible only from the lower boundary, *i.e.* when $\chi(\mathbf{Q}, \omega)$ diverges. In the simplest approximation, $\chi(\mathbf{q}, \omega)$ is calculated by ignoring the exchange part of the electron-electron interaction

in favor of Hartree-like terms only. This is known as the random phase approximation (RPA)¹³ and relates χ to the non-interacting susceptibility, χ_0 :

$$\chi_{RPA}(\mathbf{q}, \omega) = \chi_0(\mathbf{q}, \omega) / [1 - V_C(q)\chi_0(\mathbf{q}, \omega)], \quad (2)$$

where χ_0 is

$$\chi_0(\mathbf{q}, \omega) = \sum_{l', \mathbf{k}} \frac{f(\varepsilon_{l\mathbf{k}}) - f(\varepsilon_{l'\mathbf{k}+\mathbf{q}})}{\varepsilon_{l\mathbf{k}} - \varepsilon_{l'\mathbf{k}+\mathbf{q}} - \omega - i\delta} |\langle l\mathbf{k} | e^{i\mathbf{q}\mathbf{r}} | l', \mathbf{k} + \mathbf{q} \rangle|^2. \quad (3)$$

Here $f(\varepsilon)$ is the Fermi function and the matrix elements $\langle l\mathbf{k} | e^{i\mathbf{q}\mathbf{r}} | l', \mathbf{k} + \mathbf{q} \rangle$ are between Bloch functions, $|l\mathbf{k}\rangle = u_{l\mathbf{k}}(\mathbf{r})e^{i\mathbf{k}\mathbf{r}}$. If these do not have much structure as a function of \mathbf{q} , one can set them uniformly to unity, yielding the following expression for the imaginary part of χ_0 :

$$\lim_{\omega \rightarrow 0} \Im \chi_0(\mathbf{q}, \omega) / \omega = \frac{\Omega}{(2\pi)^3} \sum_{l'} \int \frac{dL_{\mathbf{k}}}{|\mathbf{v}_{l\mathbf{k}} \times \mathbf{v}_{l', \mathbf{k}+\mathbf{q}}|}, \quad (4)$$

where the line $L_{\mathbf{k}}$ is the intersection of the two surfaces defined by $\varepsilon_{l\mathbf{k}} = 0$ and $\varepsilon_{l'\mathbf{k}+\mathbf{q}} = 0$ (the Fermi energy is set to zero). Eq. 4 correctly suggests that a Fermi surface nesting, that is, a Fermi surface topology such that the length of the line $L_{\mathbf{k}}$ is particularly large at some \mathbf{Q} , should lead to a peak in $\lim_{\omega \rightarrow 0} \Im \chi_0(\mathbf{Q}, \omega) / \omega$. This is correct, but misses several important points. First, as Eq. 4 indicates, a strong maximum also requires small and/or nearly parallel $\mathbf{v}_{l\mathbf{k}}$ and $\mathbf{v}_{l', \mathbf{k}+\mathbf{q}}$ along $L_{\mathbf{k}}$. Second, it is the real, and not the imaginary part of the static susceptibility that defines a CDW instability (at $\omega = 0$, $\Im \chi_0$ vanishes). In contrast to $\Im \chi_0$, which indeed depends only on electronic characteristics near the Fermi surface, $\Re \chi_0$ collects information from an energy window of the order of the band width (which follows from Eq. 3, taking into account that $\int dE/E$ diverges at large arguments).

Finally, one should keep in mind that a divergence of the electronic susceptibility signals an instability of the system with respect to spontaneous formation of a CDW *even if the nuclei are clamped to their high-symmetry positions*. Of course, if released, the nuclei would shift as well. However, divergence of χ is a substantially more severe criterion than the soft mode condition, which is that the frequency of a particular phonon mode at some wave vector becomes zero. This latter condition defines an instability toward the freezing in of a particular periodic pattern of ionic displacement, which is the only CDW that is actually observed in real systems.

Phonon frequencies are related to the dielectric function via the so-called Pick-Cohen-Martin formula¹⁴. Here we give this formula in a simplified form for an elemental solid:

$$\begin{aligned} D_{\alpha\beta}(\mathbf{q}) &= \tilde{D}_{\alpha\beta}(\mathbf{q}) - \tilde{D}_{\alpha\beta}(0), \\ \tilde{D}_{\alpha\beta}(\mathbf{q}) &= \sum_{\mathbf{G}, \mathbf{G}'} |\mathbf{q} + \mathbf{G}|^2 V_C(\mathbf{q} + \mathbf{G})(\mathbf{q} + \mathbf{G})_{\alpha} \times \\ &\quad \epsilon^{-1}(\mathbf{q} + \mathbf{G}, \mathbf{q} + \mathbf{G}')(\mathbf{q} + \mathbf{G}')_{\beta} V_C(\mathbf{q} + \mathbf{G}'), \end{aligned} \quad (5)$$

where $D_{\alpha\beta}(\mathbf{q})$ is the dynamical matrix and α, β are Cartesian indices. It is clear that an eigenvalue of this matrix can soften and eventually become zero even if the macroscopic dielectric function^{15,16}:

$$\epsilon(\mathbf{q}) = 1 / [\epsilon^{-1}(\mathbf{q} + \mathbf{G}, \mathbf{q} + \mathbf{G}')]_{00} \quad (6)$$

does not diverge. Here and above, the dielectric function $\epsilon^{-1}(\mathbf{q} + \mathbf{G}, \mathbf{q} + \mathbf{G}')$ differs from ϵ_{RPA}^{-1} in that it includes the so-called local field effects: Umklapp processes and the exchange-correlation interaction between electrons. Formally, it is written (neglecting for simplicity the band indices) as:

$$\begin{aligned} \epsilon^{-1}(\mathbf{q} + \mathbf{G}, \mathbf{q} + \mathbf{G}') &= \delta_{\mathbf{G}\mathbf{G}'} + \sum_{\mathbf{G}_1} V_C(\mathbf{q} + \mathbf{G})\chi_0(\mathbf{q} + \mathbf{G}, \mathbf{q} + \mathbf{G}_1) \otimes \\ &\quad [\delta_{\mathbf{G}_1\mathbf{G}'} - \sum_{\mathbf{G}_2} \{\delta_{\mathbf{G}_1\mathbf{G}_2} V_C(\mathbf{q} + \mathbf{G}_1) - I_{XC}(\mathbf{q} + \mathbf{G}_1, \mathbf{q} + \mathbf{G}_2)\}\chi_0(\mathbf{q} + \mathbf{G}_2, \mathbf{q} + \mathbf{G}')]^{-1} \end{aligned} \quad (7)$$

(in these expressions, matrix inversion is with respect to the reciprocal lattice vector indices), where $I_{XC}(\mathbf{r}, \mathbf{r}') = \delta^2 E_{XC} / \delta \rho(\mathbf{r}) \delta \rho(\mathbf{r}')$ is the exchange correlation kernel [note that in the LDA $I_{XC}(\mathbf{r} - \mathbf{r}') = \delta(\mathbf{r} - \mathbf{r}') I_{XC}(\mathbf{r})$, and thus $I_{XC}(\mathbf{q} + \mathbf{G}, \mathbf{q} + \mathbf{G}') = I_{XC}(\mathbf{G} - \mathbf{G}')$].

Therefore, several separate questions must be posed: 1) Does the geometry of the Fermi surface provide nesting in the sense of a strong maximum of Eq.4? 2) Is there a peak in the real part of χ_0 , as defined in Eq.3 at the wave

vector corresponding to the observed CDW and if so, is it related to any nesting-derived structure in $\Im \chi(\mathbf{q}, 0)$? 3) Is there a divergence in $\epsilon(\mathbf{q})$ as defined by Eq.6? 4) If the previous answer is no, is there a soft mode (zero eigenvalue) in Eq. 5?

Below we present numerical density functional calculations that provide answers to the first two questions and supply information allowing for reasonable conjecture about answers to the last two. The substance of our

findings is that there is only weak nesting in this system, and at the “wrong” wave vector. While $\Re\chi_0$ does have a broad maximum at the CDW wave vector, it is likely too small to account for the CDW instability. Lacking full linear response calculations, we cannot exclude with certainty an electronic instability in $\epsilon(\mathbf{q})$ (Eq. 6), due to local field effects (exchange-correlation and Umklapp) beyond plain RPA, but it is more likely that the instability appears only after electron-ion interactions are explicitly taken into account (Eq. 5). Experiment further supports our contention as only the phonon corresponding to the actual CDW is observed to soften, whereas, if $\epsilon(\mathbf{q})$ were to diverge at some \mathbf{q} , *all* phonons would soften at this vector.

To illustrate the last point we note that χ_{RPA} itself can have a peak, but obviously cannot diverge (Eq. 2). Furthermore, including the exchange-correlation interaction between electrons within DFT, but without Umklapp processes, gives

$$\chi_{DFT}(\mathbf{q}, 0) = \frac{\chi_0(\mathbf{q}, 0)}{[1 + \{V_C(q) - I_{XC}(q)\}\chi_0(\mathbf{q}, 0)]} \quad (8)$$

This expression cannot diverge either. Finally, it can be shown that, generally speaking, the Umklapp processes tend to *lower* the electronic dielectric constant¹². Since $\epsilon(\mathbf{q}, \omega)$ can become unstable only by passing from a negative quantity to a positive one, there can be no CDW formation at any value of \mathbf{q} . Non-local correlation effects neglected by DFT may be instrumental in creating an instability beyond Eq. 8, but it is physically more likely that the electron-ion matrix elements, which can naturally have strong \mathbf{q} -dependence, account for the CDW instability through their effect on the dynamical matrix. In fact, this is consistent with some early conjectures based on simplified tight-binding calculations^{11,17}. In these works, a strong phonon softening was observed at the correct wave vector, but only when electron-ion interactions were accounted for. The authors of both works conclude, correctly, that this softening is not simply related to FS geometry, but stay short of excluding weak FS nesting as an essential factor. As we will show, no relevant nesting exists in NbSe₂, and, therefore, it cannot play any role in the CDW instability.

II. ELECTRONIC STRUCTURE

Our calculations were carried out using a full-potential, augmented plane wave plus local orbital (APW+lo) scheme¹⁸. The exchange-correlation potential was approximated by a local density approximation (LDA) parameterization¹⁹ and the muffin-tin radii were set to 2.3 (Nb) and 2.2 (Se) with a value of 7.0 for RKmax. We found small but important differences between calculations with and without the spin-orbit interaction. Except where explicitly noted, we include spin-orbit coupling using a second variational method for all calculations. The structure shown in Fig. 1 displays the unit cell

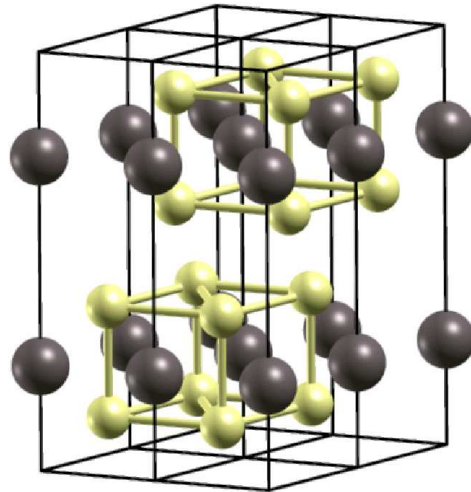


FIG. 1: The crystal structure of NbSe₂, showing the two distinct layers that make up the unit cell. Each Nb ion sits in a hexagonal mirror plane with three Se neighbors above and below, forming a network of distorted edge-sharing octahedra.

of NbSe₂. It is comprised of two formula units arranged in layers, each layer containing a hexagonal Nb plane sandwiched between two shifted hexagonal Se planes. We used the experimentally measured lattice constants²⁰, ($a=3.44 \text{ \AA}$ and $c=12.55 \text{ \AA}$), which agrees well with other reports^{21,22,23} and we relaxed the Se ions to their lowest energy positions along the c axis ($z=0.1183c$). This position is in good agreement with all experimental reports ($z = 0.116 - 0.118c$)^{20,21,22}, except Ref. 23, which gives $z = 0.125c$. Our relaxation resulted in a Se-Se interplanar distance of 3.57 \AA which can be compared with the Nb-Se intralayer distance of 2.59 \AA . Based on these separations, we expect an anisotropic band structure with rather strong interplanar coupling. To calculate the non-interacting susceptibility of Eq. 3, we used a direct summation over a very fine mesh of $73 \times 73 \times 7 \sim 40,000$ k points in the BZ, and a Fermi temperature smearing of $T=10 \text{ meV}$.

A. Band Structure

Our band structure (Fig. 2) exhibits some differences from previous full potential calculations,^{6,8} giving rise to differences in the resulting Fermi surfaces. The discrepancies are most likely due to a large difference in Se positions: $z=0.134c$ in Refs. 6,8 compared to our relaxed height of $z=0.118c$. We were not able to identify an experimental paper reporting such high Se positions.

We observe two classes of bands near the Fermi energy - the first is the fully antibonding Se p_z band, which,

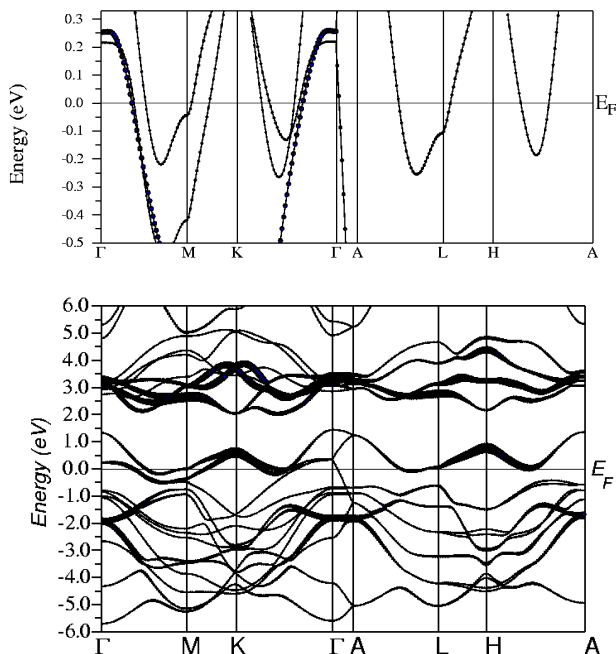


FIG. 2: (color online) The band structure of NbSe₂. *Top*: A closeup of the bands around the Fermi energy, neglecting spin-orbit coupling. The highlighted bands are of Se p_z character and cross the Nb bands without hybridization. *Bottom*: The full band structure, including the spin-orbit interaction which relieves the Nb band degeneracy in the $k_z = \pi/c$ plane. The highlighted bands are of combined $x^2 - y^2/xy$ character

by parity, does not hybridize with the z -even d -orbitals of Nb ($d_{x^2-y^2}$, d_{xy} , and d_{z^2-1}) in the $k_z=0$ plane, and does not hybridize with the z -odd Nb d orbitals in the $k_z = \pi/c$ plane. In Fig. 2a, a close-up of the band structure without spin-orbit interactions is shown. The p_z band is highlighted with filled circles and can be seen crossing and re-crossing the Nb band in the $\Gamma - K - M$ plane without mixing, despite a nearly perfect energetic degeneracy. In the $A - L - H$ plane, the range of the figure no longer includes the p_z band which has dropped nearly 2 eV in energy. This rather dramatic energy lowering can be traced to bonding-antibonding interactions between unit cells. The width of the Se p band complex (-6.0 eV to 0.5 eV) is determined by the energy difference between the bonding and anti-bonding configurations of the four p_z orbitals along the c -axis within the (two layer) unit cell and between the cells themselves. In the $k_z=0$ plane, antibonding p_z orbitals in adjacent unit cells are antibonding with each other, pushing the energy of the single fully anti-bonding p_z band up to the Fermi level. In the $k_z = \pi/c$ plane, the relationship between adjacent-cell p_z orbitals becomes bonding, the band is lowered, and the Fermi crossing is removed. Fig. 3 shows the antibonding configuration of the p_z orbitals at the Γ and A points, with arrows indicating the crucial interactions between cells.

The second class of bands consists of one Nb d band,

which, like the p_z orbitals, is split in the $k_z=0$ plane, by bonding-antibonding interactions both within and between unit cells. In Fig. 3, spheres representing the Nb d_{z^2-1} orbital (or equally the other z -even orbitals, $x^2 - y^2$ and xy) are shown in fully bonding and fully antibonding configurations at the Γ point. By contrast, in the $k_z = \pi/c$ plane (A point shown), the bonding-antibonding energy difference arising from orbital orientations within the unit cell is counteracted by interactions between cells and the band therefore remains degenerate (see Fig. 2a). In Fig. 2b, the full band structure, including spin-orbit, is shown. The spin-orbit coupling allows for p_z -Nb mixing along $\Gamma - K - M$ and removes the strict degeneracy of the Nb bands at $k_z = \pi/c$. It is tempting to identify the latter bands as simply Nb d_{z^2-1} orbitals, but is misleading: symmetry arguments, confirmed by the numerical decomposition of the LAPW bands, predict that this band should have atomic d_{z^2-1} character along the ΓA line, but $d_{x^2-y^2} + d_{xy}$ character along the KH line and mixed character elsewhere. This can be seen clearly in Fig. 2b where the $d_{x^2-y^2} + d_{xy}$ bands are highlighted and are clearly dominant near the Fermi level along some symmetry directions. One can, of course, enforce mapping of this band structure onto a one-band d_{z^2-1} TB model²⁴, but this does not reflect the character decomposition of the LAPW bands nor does it mean that this band is physically derived from actual Nb d_{z^2-1} orbitals.

B. Fermi Surfaces

In Fig. 4 our three calculated Fermi surfaces are displayed in an expanded (four total zones) Brillouin zone scheme. These surfaces are significantly different from early calculations,^{5,25,26} most notably in the existence of a third band crossing E_F . On the other hand, they are quite similar to the sketches of Ref. 6, with the difference that we designate all three surfaces as “hole-like” because the filled states are external to the drawn surfaces, whereas in Ref. 6 the third surface is called “electron-like”, presumably because the band is more than half-filled. Below we compare each FS to experimental data from angle-resolved photoemission spectroscopy (ARPES) and de Haas van Alphen (dHvA) quantum oscillation measurements.

Interlayer coupling breaks the degeneracy of the highest unfilled Nb d band and gives rise to two concentric cylindrical Fermi surfaces around the $\Gamma - A$ and $K - L$ lines of the BZ. The surfaces derived from the higher (anti-bonding) energy band (Fig. 4c) are almost dispersionless along the k_z direction, while those derived from the lower (bonding) energy band (Fig. 4b) are strongly warped. Neither of these have been seen with dHvA, which requires very pure samples to detect large orbits, but they have been consistently seen by ARPES measurements^{7,8,27,28,29} which are in very good general agreement with calculation. We will use the measure-

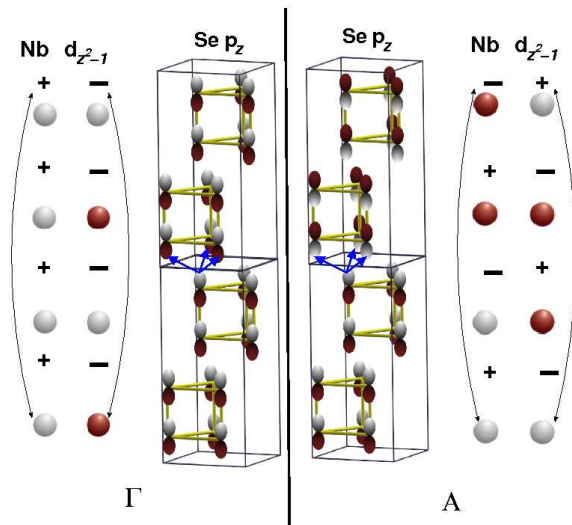


FIG. 3: (color online) A schematic showing the origin of the splitting of the antibonding p_z band and the Nb d_{z^2-1} band at two different k_z positions. The Nb ions are omitted from the structural graphic for clarity and the d_{z^2-1} orbitals have been idealized as spheres. *Left side:* At the Γ -pt, Nb d_{z^2-1} orbitals are either fully bonding or fully antibonding, and the antibonding p_z orbitals are antibonding even between cells (blue arrows). *Right side:* At the A -pt, there is no overall energy difference between bonding and antibonding Nb d_{z^2-1} configurations and the antibonding p_z orbitals are now bonding between cells. Plus signs indicate bonding and minus signs antibonding - the long black arrows connect the top-most orbital to the one that would sit above it if the cells were repeated endlessly.

ments of Rossnagel *et al*⁸, who investigated directions both parallel and perpendicular to the a - b plane, for specific comparison with our surfaces. The observed Fermi surfaces derived from the higher Nb band (Fig. 4b) show less k_z dispersion than in our calculations and consequently the pockets around $K-L$ remain rounded along their full length rather than becoming sharply triangular as ours do. The outer pockets of the lower Nb band (Fig. 4c) are not warped, consistent with our results, but the $K-L$ centered triangular pockets again appear to be more rounded. Overall there is substantial agreement between ARPES measurements and theory, particularly in terms of the observed placement and k_F of the Nb-derived FS pockets - the essential elements of interest for Fermi surface nesting.

The small pancake surface in Fig. 4a is derived from a Se $4p$ band, and has an extremely small width along the k_z direction. Very early dHvA measurements³⁰ saw this surface, but misattributed it by comparing to a band structure⁵ that didn't show the Se band crossing the Fermi energy. Later measurements by Onuki *et al*³¹ confirm the existence of these surfaces, though the authors were still apparently unaware of the calculated Se-derived Fermi surface and therefore report a discrepancy with theory. The most recent dHvA experiments⁶ clearly de-

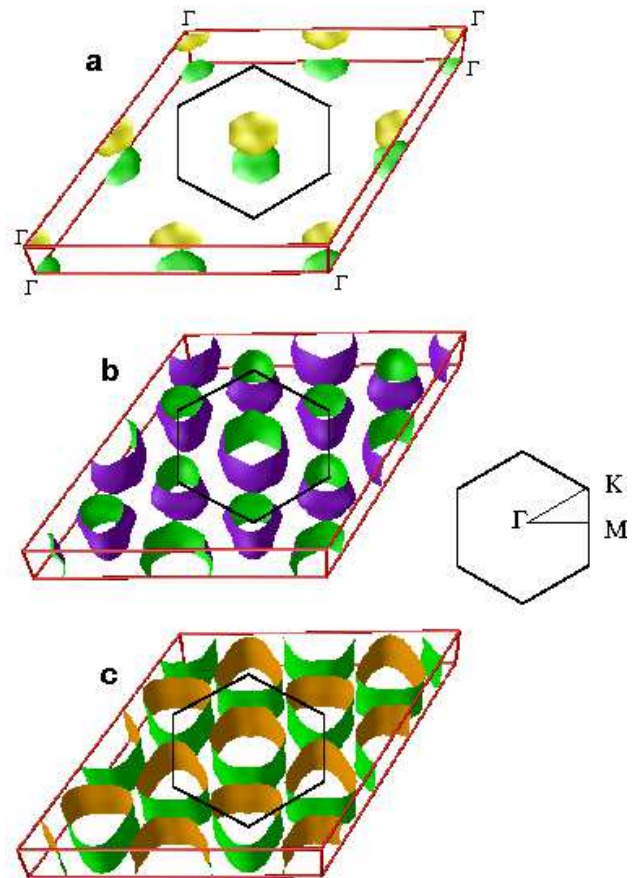


FIG. 4: The three Fermi surfaces of NbSe₂ in an extended BZ scheme with the conventional BZ indicated as a hexagon in the center of each figure. **a)** The small Se-derived (band 1) pancake surface around the Γ -point. **b)** The bonding (band 2) Nb-derived Fermi surface with strong warping along k_z . **c)** The nearly 2D anti-bonding (band 3) Nb-derived Fermi surface. The $\Gamma-K-M$ plane is at the top and bottom of each figure and the $A-L-H$ plane cuts through center.

tect and correctly identify the smallest surface, obtaining good quantitative agreement with the earlier works. ARPES measurements see a weak signal of the smallest surface^{8,27} with an in-plane area that agrees well with dHvA measurements, but with greatly exaggerated perpendicular dimension. Our calculated Se Fermi surface is larger both in- and out-of-plane with respect to dHvA measurements, but shows a smaller perpendicular width than ARPES, which is not expected to be as accurate in this direction. For comparison with available experimental data, our calculated the dHvA frequencies for the Se-derived pocket as well as all the other Fermi surfaces is shown in Table I.

Note that our calculated cross-sectional areas are noticeably different from previous work by Corcoran *et al*. This can be partially ascribed to the different Se position in their calculations. However, there were also

| | dHvA frequency (T) |
|---------------------------|--------------------|
| Band 1 | |
| (001) | 4498.4 |
| ($\bar{1}\bar{2}0$) | 472.1 |
| Band 2 | |
| $\Gamma - A$ (Γ) | 6269.9 |
| $\Gamma - A$ (A) | 8605.6 |
| $K - L$ (Γ) | 3199.0 |
| $K - L$ (A) | 5110.9 |
| Band 3 | |
| $\Gamma - A$ (Γ) | 9362.6 |
| $\Gamma - A$ (A) | 9046.6 |
| $K - L$ (Γ) | 7807.2 |
| $K - L$ (A) | 7085.2 |

TABLE I: The calculated dHvA frequencies of NbSe₂. Bands two and three have two separate surfaces, designated in the Table by the axis that runs through their centers $\Gamma - A$ or $K - L$. The two extremal orbits for each surface in a (001) field occur in the $\Gamma - K - M$ and $A - L - H$ planes, indicated by Γ and A respectively in the Table. For the Se pancake surface, the frequency was also calculated for an in-plane field direction ($\bar{1}\bar{2}0$).

probably too few k -points to ensure an accurate area calculation. Because of the simple shape of the Fermi surfaces, one can calculate their volumes from the extremal cross-section, assuming a full cylindrical symmetry for the Se pocket (which yields $V \approx S_{xz} \sqrt{\pi S_{xy}}$), and using a trapezoidal integration for the open pockets ($V \approx [S_1 + S_2]\pi/c$). Applying this procedure to Corcoran's numbers we obtain a violation of the Luttinger theorem of the order of more than 1%, while our method³² gives the correct total number of electrons with an error of less than 0.01%.

While ARPES data on the Nb Fermi surfaces agrees well with our calculations, the de Haas-van Alphen area for the Se pocket (the only one measured so far) differs by nearly 4000 T for the largest orbit and 500 T for the smallest one. However, due to the large effective mass for this pocket, a relatively minor charge transfer of only 0.02 electrons from this band to the Nb bands is needed to bring the cross-sections into agreement. The geometry of the large Nb cylinders would not be changed in any important way with such a transfer. Therefore, we can safely use the calculated band structure to evaluate the nesting effects and susceptibility in NbSe₂.

The small pancake FS, although it carries little DOS and is probably not important for superconductivity or CDW formation, plays an important role in transport. We have calculated the Fermi velocities and plasma frequencies for both in-plane and perpendicular directions. A decomposition by band, as shown in Table II), reveals that while the pancake (band 1) contributes barely 5% of the total DOS, it is carrying more than three quarters of the total current in the c direction, and is responsible

| FS sheet | DOS (states/Ry) | ω_{px} (eV) | ω_{pz} (eV) | v_{Fx} (10^8 cm ⁻¹) | v_{Fz} (10^8 cm ⁻¹) |
|---------------------|--------------------|-----------------------|-----------------------|---|---|
| Band 1 $\Gamma - A$ | 3.8 | 0.40 | 2.16 | 0.10 | 0.53 |
| Band 2 $\Gamma - A$ | 9.9 | 1.63 | 0.78 | 0.23 | 0.11 |
| Band 2 $K - L$ | 19.7 | 1.65 | 0.86 | 0.18 | 0.09 |
| Band 3 $\Gamma - A$ | 11.4 | 1.60 | 0.13 | 0.22 | 0.02 |
| Band 3 $K - L$ | 29.5 | 1.85 | 0.26 | 0.16 | 0.02 |
| total | 74.2 | 3.37 | 2.46 | 0.19 | 0.14 |

TABLE II: The density of states, plasma frequencies and Fermi velocities for the 5 sheets of the Fermi surface.

for the relatively 3D character of the resistivity in this compound. If, as discussed above, we adjust the relative position of the Se pancake and the other bands, ω_{pz}^2 for this band would drop by less than 50%, so that it would still contribute about as much as all other bands together to the transport across the planes. This, has important ramifications for superconductivity: any experiment related to tunneling (Josephson contacts, Andreev reflection *etc.*) in the direction perpendicular to the plane will probe mostly the Se pancake band which carries a very small part of the Cooper pairs and may actually have a reduced superconducting gap (reference to ARPES). Furthermore, if there is any difference between the superconducting properties of different Nb-derived sheets, this may also manifest itself in a nontrivial way in such tunneling, since the third band has nearly zero k_z dispersion and its contribution to the c -transport is nearly negligible (See Table II).

We now discuss the scenarios previously suggested as candidates for nesting at \mathbf{Q}_{CDW} and compare them quantitatively with our theoretical Fermi surfaces. The six symmetry-equivalent saddle points along the $\Gamma - K$ directions (not shown) are separated by $\mathbf{Q}_{SP1} = (\frac{1}{6}, \frac{1}{6}, 0)$ or by $\mathbf{Q}_{SP2} = (\frac{1}{2}, 0, 0)$, neither of which is near \mathbf{Q}_{CDW} . Moreover, the calculated saddle point is approximately 150 meV beneath the Fermi energy, and although ARPES measurements⁷ show that band renormalization reduces the depth to only 50 meV, this is still too great an energy compared to the $k_B T_{CDW} = 3$ meV required for the saddle point theory of Rice and Scott⁹, as has been noted by others⁸. There have been suggestions that self-nesting between the parallel flat edges of the central hexagonal Fermi surfaces around $\Gamma - A$ could be responsible for the CDW instability⁷. Our calculations show that only the smaller (second band) surface is oriented correctly to produce self-nesting along $\Gamma - M$; the larger surface would self-nest along $\Gamma - K$. The spanning vector between the faces of the inner surface is (0.41, 0, 0) which is too large in comparison to \mathbf{Q}_{CDW} (that of the outer surface is, of course, even larger). A similar conclusion was reached in Refs. 8 and 28. Furthermore, due to substantial k_z dispersion in the second pocket, good nesting does not occur along the full length of the cylinder, substantially reducing L_k in Eq. 4 and thereby diminishing the contribution to χ . Rossnagel *et al*⁸, noting this dispersion

along k_z , suggested that the broad peak calculated^{11,17} in $\chi_0(\mathbf{Q}_{CDW}, 0)$ is due to imperfect (weak) nesting between these warped cylindrical surfaces themselves (self-nesting) and between neighboring cylinders. Our calculation of $\chi(\mathbf{q}, 0)$ shows that such a scenario is not manifested for NbSe₂ (see Section III). It has been recently postulated²⁹ that the $K-L$ centered cylinders, which are smaller than those around $\Gamma-A$, might nest at approximately the right wave vector. The cross-sections of these cylinders, however, are not circles but are rounded triangles with flat edges oriented at 120° with respect to one another, making such nesting highly unlikely. The only apparent strong nesting possibility, according to our calculations occurs between the flat triangular edges of the $K-L$ cylinders and the parallel flat edges of the central hexagonal pocket, $\mathbf{Q} = (\frac{1}{3}, \frac{1}{3}, 0)$. In the next section, we will show that it is indeed this nesting that produces the highest peaks in the imaginary part of the susceptibility. We reiterate here that FS nesting causes peaks in the imaginary part of χ_0 , while the real part of χ_0 , which is the essential quantity for CDW formation, draws from a much larger energy range and may have features entirely unrelated to FS topology.

III. NON-INTERACTING SUSCEPTIBILITY

The calculated real and imaginary parts of the non-interacting susceptibility are shown in Fig. 5. The matrix elements of Eq. 3 have been set to $\delta_{ll'}$ so that no inter-band contributions are taken into account. The effects of these terms turn out to be quite weak as we will show later in the text. The clear peaks in $\Im\chi_0$ indicate nesting at $\mathbf{q} = (\frac{1}{3}, \frac{1}{3}, 0)$ and by symmetry, at $\mathbf{q} = (\frac{2}{3}, \frac{2}{3}, 0)$. These correspond to translating the central pocket from Γ to K . This results in partial nesting between the hexagonal and triangular pockets, as well as between two triangular pockets with different orientations. Since the pockets can slide around inside one another, the peak is broad and, in fact, is not truly a single peak, but a composite peak composed of three separate peaks *near* $\mathbf{q} = K$, and corresponding to separate nestings of the three edges of each triangle. Assuming that the triangular surfaces are, in actuality, more rounded as indicated by ARPES, we expect these three peaks to further “smear” into one central peak. There is no indication of any other nesting and, most significantly, there is no peak whatsoever at $\mathbf{q} = \mathbf{Q}_{CDW}$. This situation differs from that of isostructural NbTe₂ where a strong peak in $\Im\chi(\mathbf{q}, 0)$ does exist³³ at \mathbf{Q}_{CDW} , though we note that such a peak cannot be taken as evidence that nesting contributes to CDW formation without a calculation of $\Re\chi(\mathbf{q}, 0)$. Unless the true fermiology of NbSe₂ differs significantly from our calculations (and comparison with experiment strongly suggests that it does not), there is *no evidence* of a FS nesting contribution to CDW formation at all.

The peaks in the imaginary part of the susceptibility are always present in the real part because E_F is

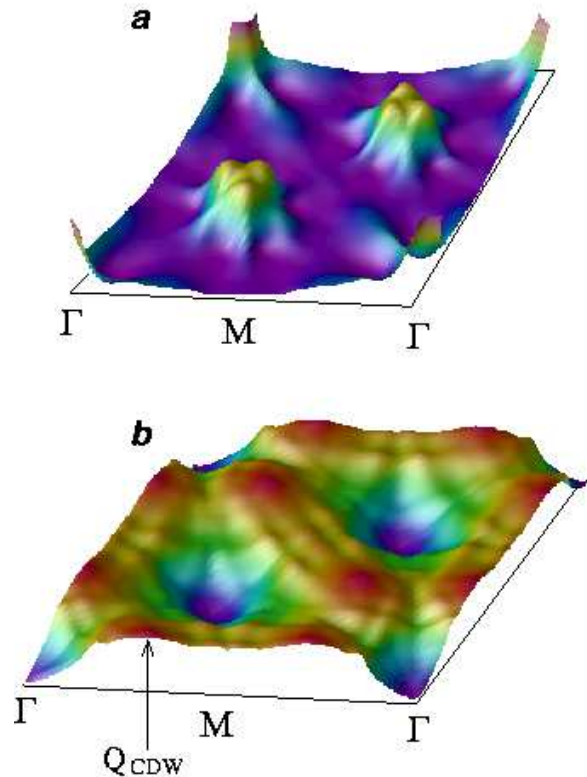


FIG. 5: The non-interacting susceptibility of NbSe₂. a) The imaginary part exhibits FS nesting driven peaks at $\mathbf{Q} = (\frac{1}{3}, \frac{1}{3}, 0)$. The plane at the bottom is a guide for the eye and corresponds to the lowest value of $\Im\chi_0$. b) The real part has very weak peaks at \mathbf{Q}_{CDW} that come from energy intervals away from E_F . (see text). The plane corresponds to the lowest value of $\Re\chi_0$, which is also the density of states at the Fermi level.

part of the sampled energy range, but these can be either emphasized or overshadowed by contributions from other energies. In the case of NbSe₂, the peaks at K are no longer even visible and broad maxima appear instead along the $\Gamma-M$ line. These do occur approximately at \mathbf{Q}_{CDW} , but are unlikely to be strong enough to produce a CDW instability. A two-dimensional plot of $\Re\chi_0$ along $\Gamma-M$ is shown in Fig. 6, with the position of the observed CDW wave vector indicated. The highest point along this curve is 33.5 Ryd⁻¹ above the lowest point, $\Re\chi_0(0) = N(E_F) = 70.3$ Ryd⁻¹, and occurs at $\mathbf{q} = (0.31, 0, 0)$ which is, in fact, rather near \mathbf{Q}_{CDW} . Fig. 6 includes a band-by-band decomposition of the contributions to $\Re\chi_0(\mathbf{q})$ along $\Gamma-M$ showing almost no contribution at all from the Se-derived band and a rather peaked contribution from the antibonding Nb band, but at a wave vector quite different from \mathbf{Q}_{CDW} . Finally, we have included a plot of $\Re\chi_0(\mathbf{q})$ with both intra- and

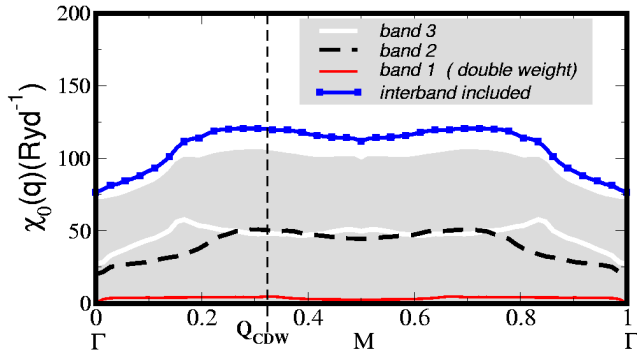


FIG. 6: $\Re\chi_0(\mathbf{q})$ along the Γ – M line of the Brillouin zone. The total is shown in shaded grey with the contributions from each individual band delineated by different lines. The height of band 1 has been multiplied by two to make it visible above the x-axis. The topmost line includes non-diagonal (interband) contributions.

interband matrix elements set to unity in Eq. 3. This exaggerates the contributions of interband transitions, but gives a rough idea of their effect on the susceptibility. We find an overall shift upward of the entire spectrum but no particular sharpening of the peaks. Along Γ – M , our susceptibility somewhat resembles that of Ref. 10, but the suggestion that the broad peak is due to self-nesting of the central pocket is clearly unjustified as no such peak appears in $\Im\chi_0$.

To isolate the true source of the (weak) maxima, we calculate a function,

$$F(x, y) = \int \delta(\epsilon_{\mathbf{k}} - x) \delta(\epsilon_{\mathbf{k}+\mathbf{q}} - y) d\mathbf{k}, \quad (9)$$

from which the susceptibility can be recovered through

$$\chi(\mathbf{q}) = \int_{-\infty}^{\epsilon_F} dx \int_{\epsilon_F}^{\infty} dy \frac{F(x, y)}{x - y} \quad (10)$$

By adjusting the limits of the integrals in Eq. 10, the energy interval that gives rise to any given feature in χ_0 can be isolated. For a very small interval near the Fermi energy, all the features of $\Im\chi_0$ are reproduced, including

the dominant feature at K . However, for energy intervals away from the Fermi energy, there is little or no contribution to $\chi_0(K)$, with the result that the real part of χ_0 has a minimum there when all energies are taken into account. Much of the contribution to $\Re\chi_0$ comes from eigenvalues in the energy range $|\epsilon_{\mathbf{k}+\mathbf{q}} - \epsilon_{\mathbf{k}}| > 0.02$ Ryd. This reinforces in a rather dramatic way our earlier assertion that one should not expect a CDW instability to stem from FS nesting.

IV. CONCLUSIONS

We have calculated the real and imaginary parts of the non-interacting susceptibility as a function of wave vector throughout the Brillouin zone. The real part of χ_0 exhibits very weak peaks near \mathbf{Q}_{CDW} that are unlikely to be strong enough alone to cause a CDW instability. The main contributions to these peaks come from an energy range *not* near E_F , indicating that FS nesting is irrelevant. A direct calculation of $\Im\chi_0(\mathbf{q})$ confirms that there is absolutely no FS nesting at \mathbf{Q}_{CDW} , although peaks due to nesting along $\mathbf{q} = (\frac{1}{3}, \frac{1}{3}, 0)$ are evident. It can therefore be definitively stated that Fermi surface nesting contributes nothing to CDW instability in NbSe₂. This is indicative of the more general, but often overlooked fact that Fermi surface nesting has an immediate effect only on the imaginary part of susceptibility, relevant, for instance, for the spin excitation spectrum, but not to CDW formation. The latter is defined by the structure of the real part of susceptibility, which is not directly affected by the Fermi surface nesting. More precisely, the effect of nesting on $\Re\chi_0(\mathbf{q}, \omega)$ occurs in a very small part of the total relevant energy range (which is of the order of electronvolts rather than Kelvins), and if the electronic structure changes qualitatively within this range for a given system, which is nearly always the case, then nesting cannot be considered a primary mechanism of CDW formation.

Acknowledgments

We would like to acknowledge several helpful and enlightening discussions with Girsh Blumberg and Aleksej Mialitsin. Research at NRL is supported by the Office of Naval Research.

¹ V. L. Ginzburg, Phys. Lett. **13**, 101 (1964).
² B. T. Matthias, T. H. Geballe, and V. B. Compton, Rev. Mod. Phys. **35**, 1 (1963).
³ E. Revolinsky, E. P. Lautenschlager, and C. H. Armitage, Solid State Comm. **1**, 59 (1963).
⁴ J. A. Wilson, F. J. Di Salvo, and S. Mahajan, Phys. Rev. Lett. **32**, 882 (1974).
⁵ L. F. Mattheiss, Phys. Rev. Lett. **30**, 784 (1973).
⁶ R. Corcoran, P. Meeson, Y. Onuki, P-A. Probst, M.

Springford, K. Takita, H. Harima, G. Y. Guo, and B. L. Gyorffy, J. Phys. Condens. Matter. **6**, 4479 (1994).
⁷ T. Straub, T. Finteis, R. Claessen, P. Steiner, S. Hufner, P. Blaha, C. S. Oglesby, and E. Bucher, Phys. Rev. Lett. **82**, 4504 (1999).
⁸ K. Rossnagel, O. Seifarth, L. Kipp, M. Skibowski, D. Voss, P. Kruger, A. Mazur, and J. Pollmann, Phys. Rev. B. **64**, 235119 (2001).
⁹ T. M. Rice and G. K. Scott, Phys. Rev. Lett. **35**, 120

- (1975).
- ¹⁰ N. J. Doran, B. Ricco, M. Schreiber, D. Titterington, and G. Wexler, *J. Phys. C: Solid State Phys.* **11**, 699 (1978).
 - ¹¹ N. J. Doran, *J. Phys. C: Solid State Phys.* **11**, 959 (1978).
 - ¹² O. V. Dolgov, D. A. Kirzhnits, and E. G. Maksimov, *Superconductivity, Superdiamagnetism and Superfluidity* (MIR Publ., Moscow, 1987).
 - ¹³ P. Nozieres and D. Pines, *Phys. Rev.* **109**, 741 (1958).
 - ¹⁴ R. M. Pick, M. H. Cohen, and R. M. Martin, *Phys. Rev. B* **1**, 910 (1970).
 - ¹⁵ S. L. Adler, *Phys. Rev.* **126**, 413 (1962).
 - ¹⁶ N. Wiser, *Phys. Rev.* **129**, 62 (1963).
 - ¹⁷ K. Motizuki and E. Ando, *J. Phys. Soc. Japan* **8**, 2849 (1983).
 - ¹⁸ P. Blaha, K. Schwarz, G. K. H. Madsen, D. Kvasnicka, and J. Luitz, *Wien2k* (2002), iSBN 3-9501031-1-2.
 - ¹⁹ J. P. Perdew and Y. Wang, *Phys. Rev. B* **45**, 13244 (1992).
 - ²⁰ M. Marezio, P. D. Dernier, A. Menth, and G. W. Hull Jr., *J. Solid State Chem.* **4**, 425 (1972).
 - ²¹ V. L. Kalikhman, *Inorg. Mat.* **19**, 957 (1983).
 - ²² B. E. Brownand and D. J. Beerntsen, *Acta. Cryst.* **18**, 30 (1965).
 - ²³ K. Selte and A. Kjekshus, *Acta. Chem. Scand.* **18**, 697 (1964).
 - ²⁴ R. L. Barnett, A. Polkovnikov, E. Demler, W-G. Yin, and W. Ku, *cond-mat/0508590* (2005).
 - ²⁵ C. Y. Fong and M. L. Cohen, *Phys. Rev. Lett.* **32**, 720 (1974).
 - ²⁶ G. Wexler and A. M. Woolley, *J. Phys. C: Solid State Phys.* **9**, 1185 (1976).
 - ²⁷ T. Yokoya, T. Kiss, A. Chainani, S. Shin, M. Nohara, and H. Takagi, *Science* **294**, 2518 (2001).
 - ²⁸ T. Kiss, T. Yokoya, A. Chainani, S. Shin, M. Nohara, and H. Takagi, *Physica B* **312**, 666 (2002).
 - ²⁹ T. Valla, A. V. Federov, P. D. Johnson, P-A. Glans, C. McGuinness, K. E. Smith, E. Y. Andrei, and H. Berger, *Phys. Rev. Lett.* **92**, 086401 (2004).
 - ³⁰ J. E. Graebner and M. Robbins, *Phys. Rev. Lett.* **36**, 422 (1976).
 - ³¹ Y. Onuki, I. Umehara, T. Ebihara, N. Nagai, and K. Takita, *J. Phys. Soc. Japan* **61**, 692 (1991).
 - ³² C. A. Howells, M. D. Johannes, and I. I. Mazin, To be published.
 - ³³ C. Battaglia, J. Cercellier, F. Clerc, L. Despont, M. G. Garnier, C. Koitzsch, P. Aebi, H. Berger, L. Forro, and C. Ambrosch-Draxl, *cond-mat/0508097* (2005).